frontiers | Frontiers in Physics

TYPE Original Research
PUBLISHED 29 November 2023
DOI 10.3389/fphy.2023.1303247

OPEN ACCESS

EDITED BY
Iain Sedgwick,
Rutherford Appleton Laboratory,
United Kingdom

REVIEWED BY
Carl Grace,
Berkeley Lab (DOE), United States
Vandana Sharma,
Indian Institute of Technology
Hyderabad, India

*CORRESPONDENCE
Marcin Sikorski,
marcin.sikorski@xfel.eu
Marco Ramilli,
marco.ramilli@xfel.eu

†These authors have contributed equally to this work and share first authorship

RECEIVED 27 September 2023
ACCEPTED 13 November 2023
PUBLISHED 29 November 2023

CITATION
Sikorski M, Ramilli M, de Wijn R, Hinger V, Mozzanica A, Schmitt B, Han H, Bean R, Bielecki J, Bortel G, Dietze T, Faigel G, Kharitonov K, Kim C, Koliyadu JCP, Koua FHM, Letrun R, Lopez LM, Reimers N, Round A, Sarma A, Sato T, Tegze M and Turcato M (2023), First operation of the JUNGFRAU detector in 16-memory cell mode at European XFEL. *Front. Phys.* 11:1303247. doi: 10.3389/fphy.2023.1303247

First operation of the JUNGFRAU detector in 16-memory cell mode at European XFEL

Marcin Sikorski[1*†], Marco Ramilli[1*†], Raphael de Wijn[1], Viktoria Hinger[2], Aldo Mozzanica[2], Bernd Schmitt[2], Huijong Han[1], Richard Bean[1], Johan Bielecki[1], Gábor Bortel[3], Thomas Dietze[1], Gyula Faigel[3], Konstantin Kharitonov[1], Chan Kim[1], Jayanath C. P. Koliyadu[1], Faisal H. M. Koua[1], Romain Letrun[1], Luis M. Lopez[1], Nadja Reimers[1], Adam Round[1], Abhisakh Sarma[1], Tokushi Sato[1], Miklós Tegze[3] and Monica Turcato[1]

[1]European XFEL, Schenefeld, Germany, [2]Paul Scherrer Institut, Villigen, Switzerland, [3]Wigner Research Centre for Physics, Institute for Solid State Physics and Optics, Budapest, Hungary

The JUNGFRAU detector is a well-established hybrid pixel detector developed at the Paul Scherrer Institut (PSI) designed for free-electron laser (FEL) applications. JUNGFRAU features a charge-integrating dynamic gain switching architecture, with three different gain stages and 75 µm pixel pitch. It is widely used at the European X-ray Free-Electron Laser (EuXFEL), a facility which produces high brilliance X-ray pulses at MHz repetition rate in the form of bursts repeating at 10 Hz. In nominal configuration, the detector utilizes only a single memory cell and supports data acquisition up to 2 kHz. This constrains the operation of the detector to a 10 Hz frame rate when combined with the pulsed train structure of the EuXFEL. When configured in so-called *burst* mode, the JUNGFRAU detector can acquire a series of images into sixteen memory cells at a maximum rate of around 150 kHz. This acquisition scheme is better suited for the time structure of the X-rays as well as the pump laser pulses at the EuXFEL. To ensure confidence in the use of the *burst* mode at EuXFEL, a wide range of measurements have been performed to characterize the detector, especially to validate the detector alibration procedures. In particular, by analyzing the detector response to varying photon intensity (so called 'intensity scan'), special attention was given to the characterization of the transitions between gain stages. The detector was operated in both dynamic gain switching and fixed gain modes. Results of these measurements indicate difficulties in the characterization of the detector dynamic gain switching response while operated in *burst* mode, while no major issues have been found with fixed gain operation. Based on this outcome, fixed gain operation mode with all the memory cells was used during two experiments at EuXFEL, namely in serial femtosecond protein crystallography and Kossel lines measurements. The positive outcome of these two experiments validates the good results previously obtained, and opens the possibility for a wider usage of the detector in *burst* operation mode, although compromises are needed on the dynamic range.

KEYWORDS

hybrid detector, EuXFEL, adaptive gain, characterization, calibration

1 Introduction

The European X-ray Free-Electron Laser (EuXFEL) [4] generates high brilliance X-ray pulses at megahertz repetition rate. The pulses are grouped into bursts, also known as "trains," occurring at a rate of 10 Hz. Within each train, pulses are generated at an intra-burst frequency reaching up to 4.5 MHz. The duration of a burst is approximately 0.6 ms, followed by a 99.4 ms gap period between subsequent pulse trains. This unique time structure opens novel scientific opportunities but also poses technological and engineering challenges, particularly in the domain of X-ray detection. Three types of large, mega-pixel imaging detectors, namely, AGIPD [5], LPD [6], and DSSC [7] were developed explicitly for the EuXFEL to enable pulse-resolved measurements at megahertz repetition rate. They are at present successfully used in various types of scientific experiments and are critical components of the scientific instruments at the facility. The detectors' capability to capture images at a repetition rate of 4.5 MHz also entails a series of constraints, such as a relatively large pixel size (ranging from 200 to 500 μm), elaborate calibration procedures [6, 8, 9], large physical dimensions, and extensive support infrastructure. Therefore, the MHz detectors are frequently complemented by smaller pixelated detectors, which offer smaller pixel size, lower noise, compact/modular design, and well established calibration procedures. Among those, the JUNGFRAU detector [1–3] is currently the most widely deployed at EuXFEL. The pixel size of 75 μm combined with a relatively low noise (~80 ENC) and a dynamic range of 10^4 12 keV photons [3] make the JUNGFRAU well suited for a wide range of scientific applications, from protein crystallography [10] to spectroscopy [11].

As the JUNGFRAU was developed primarily for SwissFEL [12, 13] and synchrotron applications, its compatibility with EuXFEL's bunch structure is not optimal. The JUNGFRAU detector has so far been mostly operated at 10 Hz at EuXFEL across a number of instruments. In many cases, the signal is integrated over multiple pulses per train. Therefore, the benefit of the sub-microsecond temporal resolution offered by the MHz intra-bunch repetition rate is lost. However, due to the high signal-to-noise ratio of the detector at hard X-ray photon energies (ranging between 6 keV and 20 keV), longer integration times do not significantly compromise the performance.

Due to the detector's architecture (see Section 2.1.2), the 15 additional memory cells open the possibility of a more effective exploitation of the pulse-train structure. However, the relatively large RC time characteristic of the pixel readout architecture limits the frame rate in *burst* mode to a maximum of ~150 kHz; nevertheless its implementation remains an attractive option. For example, operating the detector in *burst* mode in pulse-resolved measurements such as protein crystallography will increase data throughput 16-fold. In addition, for experiments using low-viscosity buffer media it will offer an attractive compromise between detector performance and sample consumption. For many other types of experiments, it will improve time resolution while maintaining all the advantages of the JUNGFRAU detector.

The 16-memory-cell operation of the detector, however, requires complete characterisation and calibration procedures to be established and validated before it can be provided for user operation.

In this work, the performance of the JUNGFRAU detector operating in *burst* (16-cell) mode was studied for various detector configurations and illumination levels. Special attention was given to the transition regions between the high-, medium-, and low-gain stages. Serial femtosecond crystallography data were collected using lysozyme as a model system to enable statistical comparisons, operating the detector in fixed medium gain. Additionally, single shot Kossel line measurements were used to study the fast dynamics of single crystal materials. The quality of the data collected in *burst* mode was validated against literature data.

2 Materials and methods

2.1 The JUNGFRAU detector

JUNGFRAU is a hybrid pixel detector designed and produced at Paul Scherrer Insitut (PSI), in Villigen (CH), consisting of pixelated Application-Specific Integrated Circuits (ASICs) bump-bonded to a semiconductor sensor (current versions use Si of 320 μm or 450 μm thickness; high-Z materials such as GaAs and CdZnT are under investigation).

Each ASIC is segmented into pixels of 75 μm pitch, each featuring a charge-integrating Dynamic Gain Switching (DGS) architecture, with a dynamic range on the order of 110 dB. Each pixel has an array of 16 memory cells that can store the collected analog signal before the readout. A matrix of 256 × 256 pixels comprises a single ASIC. An array of 4 × 2 ASICs is bump-bonded to a single monolithic silicon sensor, constituting a JUNGFRAU Front-End Module (FEM) of 1,024 columns and 512 rows, for a total of about 0.5 megapixels.

Each ASIC is divided into supercolumns of 64 columns × 256 rows, whose pixel output signal is multiplexed to an individual off-chip Analog-to-Digital Converter (ADC) for digitization; the whole module is therefore read out by a total of 32 different ADCs.

The FEM is operated via a dedicated electronic component, the JUNGFRAU Master Control Board (MCB), equipped with a 40 MHz Field Programmable Gate Array (FPGA) actively controlling the ASICs, and a small processor with embedded Linux Operating System (OS) running a server allowing slow control of the module.

A third electronic component is necessary to deliver the external Transistor-Transistor Logic (TTL) signal trigger to the JUNGFRAU MCB.

Each JUNGFRAU module comprises a FEM coupled with a JUNGFRAU MCB and operates individually, running on the clock of its own FPGA; however, more modules can be simultaneously controlled and configured, and their acquisition can be syncronized with a common external trigger, allowing the operation of multi-module configurations.

2.1.1 Dynamic gain switching (DGS)

In order to comply with the dynamic range requirements of a FEL, the pixel architecture of the JUNGFRAU detector is designed with a DGS mechanism: a pixel-wise threshold comparator switches additional capacitors into the pre-amplifier feedback loop if the signal rises above a certain value (set module-wise), thus increasing the feedback capacitance and reducing the gain. In the JUNGFRAU pixels, the Correlated Double Sampling (CDS) stage (see Figure 1) is bypassed after gain switching, hence causing a sign inversion of the signal curve slope.

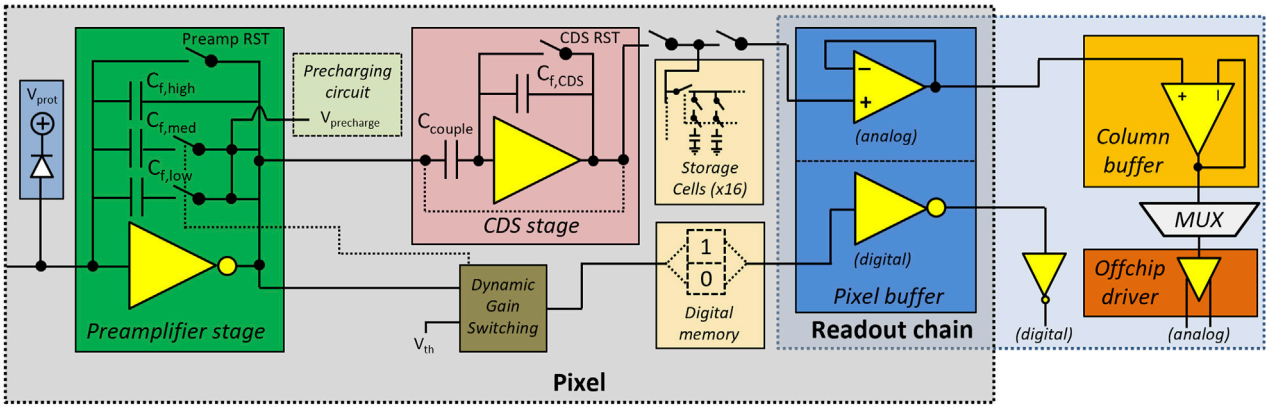

FIGURE 1
Schematics of the JUNGFRAU pixel architecture.

There are a total of three gains (respectively G0, G1, and G2) which can be independently triggered in each pixel, with relative amplification ratios:

$$R_1 = \frac{G0}{G1} \sim 30 \quad (1)$$

$$R_2 = \frac{G1}{G2} \sim 20. \quad (2)$$

During acquisition the integrated charge is temporarily stored in dedicated capacitors (memory cells) and, during the readout phase, the signal stored in each memory cell is multiplexed image-wise to one of the 32 14-bit ADCs for digitization. The state of the DGS mechanism is digitally recorded for each memory cell by changing the value of two so-called *gain bits* (00, 01, and 11 for G0, G1, and G2, respectively): this value is then appended to the ADC output.

Additionally, there is the possibility of turning the DGS mechanism off, by fixing the value of the pre-amplifier feedback capacitance to the one corresponding to G1 or G2. This operation mode is referred to as *fixed gain* mode. When operating in fixed gain mode, the CDS stage is not bypassed, therefore the gain conversion factor for $G1_{fix}$ and $G2_{fix}$ are higher with respect to their DGS counterparts.

Since the detector was primarily designed for SwissFEL and synchrotron applications [1, 13], the pixel architecture has not been optimized for MHz-class frame-rate acquisition. Its most widely employed and well-characterized operation mode is *single cell* operation, where only one of the 16 available memory cells is utilized: in this operation mode, a continuous frame rate of ~2 kHz can be achieved. This is sufficient to allow the detector to acquire at least one image per EuXFEL train and to produce useful scientific data [14–18]; however, the possibility of better exploiting the EuXFEL pulse train structure is attractive for many experiments.

2.1.2 Sixteen memory cell operation

Due to the 15 additional memory cells available in each pixel, it is possible to acquire up to 16 images in rapid succession and to read them out at the end of each measurement cycle. This is the so-called *burst* mode of operation, where pixels are operated differently from the *single cell* mode:

- In single cell mode, one memory cell is continuously connected to the memory cell bus. However, in *burst* mode the capacitors are sequentially connected during the acquisition phase and again during the readout;
- The reset of the pre-amplifier and the CDS is performed in the short time between acquisitions instead of during the long readout between trains.

The default memory cell used in single cell mode (cell 15) is the first cell in the *burst*, which is then followed by the fifteen additional cells. Both the exposure time and the dead time between two consecutive exposures can be adjusted to experimental needs. Frequently, in a similar way to single cell operation, the signal from multiple X-ray pulses is detected within a single memory cell. To allow sufficient time for the signal to settle after the reset perturbation, photons should arrive around ~1 µs after the opening of the integration gate, while, to avoid late gain switching effects, they should not arrive later than ~2 µs before the end of the integration gate. The shortest dead time between two exposures is 2.1 µs, dictated by the time needed to reset the pre-amplifier and CDS stage. Therefore, the maximum operational acquisition rate of the JUNGFRAU in *burst* mode is around 150 kHz.

2.1.2.1 Calibration of the raw data

In principle, determination of the calibration constants in *burst* mode should follow the same procedure as in single cell mode [19]. Below, we shortly outline the calibration strategy applied to data collected in *burst* mode.

2.1.2.1.1 Pedestal evaluation. The detector is equipped with two special operation modes, called *forceswitchg1* and *forceswitchg2*, which are used to estimate the pedestal value for the G1 and G2 gain stages, respectively, by forcing the pre-amplifier to switch gain. Although this procedure is used routinely for single cell operation, validation is required for *burst* mode.

Preliminary tests of the forced gain switch of the detector operated in *burst* mode, showed the presence of artefacts in the resulting pedestal values due to the very high peak current

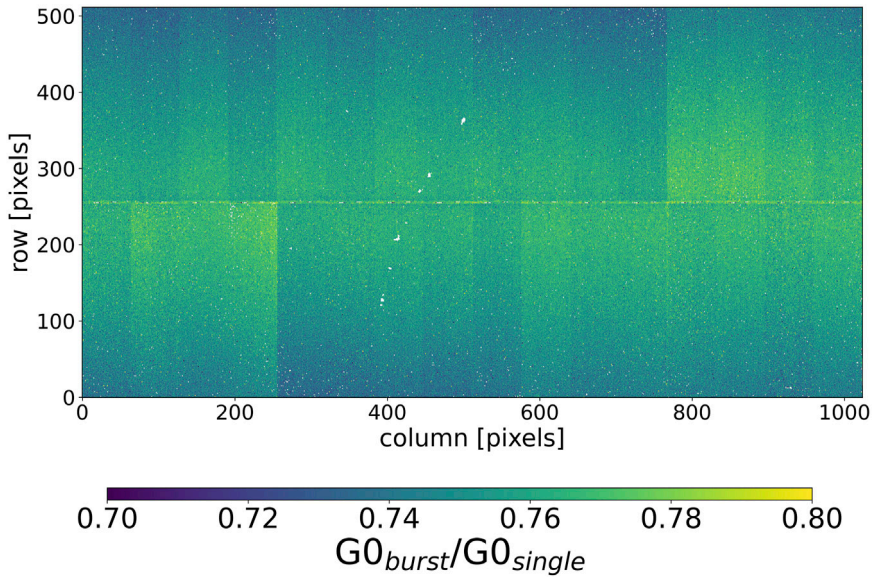

FIGURE 2
Ratio of G0 gains measured in *burst* and single memory cell configuration.

consumption during high repetition forced gain switching. Since the first memory cell connected to the bus was not yet affected, a pedestal measurement procedure has been outlined:

1. G0 pedestal values are measured by acquiring dark images with all the memory cells connected to the bus, and then calculating the average for each cell;
2. For G1 and G2 the forced gain switch is used, but only data from the *first* memory cell connected to the bus is used to calculate the pedestal value; hence, to acquire valid data for all cells, the forced switch gain measurement is repeated 16 times, each time connecting a different memory cell as first.

One of the main goals of the present study is indeed to validate this procedure.

2.1.2.1.2 Gain evaluation. Gain conversion maps for *burst mode* must be re-evaluated with respect to the single-cell mode for two main reasons:

1. The memory cells with index from 0 to 14 have, by design, a smaller capacitance than memory cell 15 (the default cell), due to space limitations in the pixel layout;
2. Memory cells are connected to the memory cell bus in turn instead of having a constant connection. This implies that the signal is smaller in *burst* mode than in single-cell mode. In fact, in the latter case the voltage written on the $C_{memorycell} + C_{bus}$ capacitance is directly presented to the pixel output voltage buffer, while in the former case the charge on the $C_{memorycell}$ is redistributed on the $C_{memorycell} + C_{bus}$, thus lowering the voltage at the pixel buffer input. This effect is illustrated in Figure 2.

In principle, the full calibration procedure outlined in [19] should not need to be repeated for all memory cells in all gain stages, as the gain ratios R_1 and R_2 do not depend on the individual memory cell, but only on the pre-amplifier (see Figure 1). Therefore, after having measured the gain G0 in *burst mode* for each memory cell, the G1 and G2 values are calculated using the gain ratios previously measured [19].

2.2 Dynamic range scan with EuXFEL beam

To validate the calibration strategies outlined in Sections 2.1.2.1.1 and 2.1.2.1.2, a JUNGFRAU detector was illuminated with X-ray pulses of varying intensity (so called 'intensity scan') to probe the detector response across at least the first two gain stages, a measurement similar to those performed in [20]. Ideally, the detector output (corrected for pedestal and gain for each memory cell) should have a linear response as a function of the impinging illumination, in particular:

- There should be no artifacts around the 'gain switching region' (GSR), i.e., the incoming photon flux range at which enough signal is generated in order to cause the pre-amplifier to switch gain;
- If gain calibration is correct, the slope of the corrected response curve should be the same for each gain stage.

2.2.1 Experimental setup

The measurements described in this document were carried out using the 4 megapixel JUNGFRAU detector (JF4M) installed at the downstream interaction region (IRD) of the SPB/SFX scientific instrument [21] at atmospheric pressure. The IRD is mainly used for serial femtosecond crystallography (SFX) experiments, therefore the detector and infrastructure design are optimised for these demands. The JF4M detector is shown in Figure 3A. It consists of eight 0.5 megapixel JUNGFRAU units arranged in two columns.

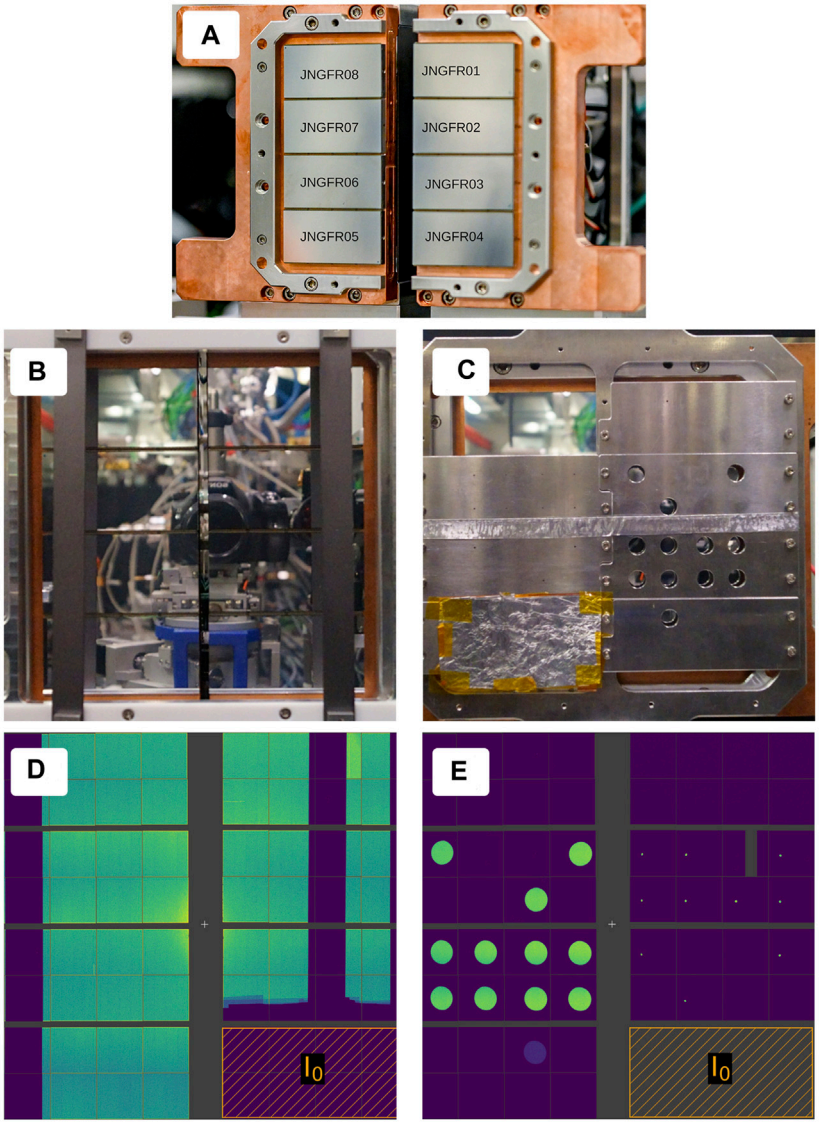

FIGURE 3
(A) The four megapixel JUNGFRAU (JF4M) detector at the SPB/SFX instrument at EuXFEL. For reference, the individual modules were labelled as JNGFR01 to JNGFR08. **(B,C)** Two types of masks used to characterize the *burst* mode. Position of the vertical tantalum bars and configuration of the aluminium panels were adjusted between various measurement. **(D,E)**: Example images acquired with both masks. Modules designated as the incident intensity monitors are marked and labelled as "I_0."

For reference, individual modules are labelled JNGFR01 to JNGFR08 (Figure 3A). At the beginning of each pulse train, the eight modules receive the same trigger signal to synchronize the start of their image acquisition to the EuXFEL light delivery. Typically, the beam not diffracted by the sample passes through the gap between the columns and interacts with the beam diagnostics downstream of the detector. Both size and position of the gap with respect to the primary X-ray beam are optimized by adjusting the horizontal position of each detector half independently.

During a typical SFX measurement, crystals are suspended in a dedicated delivery buffer and injected into the interaction point in the form of a jet. The interaction with the focused beam results in the explosion of the jet. To protect the detector from debris created during such explosions, kapton shields are installed in front of the sensor. The position of the shield can be adjusted in both horizontal and vertical directions. During the measurements reported here, the shield was replaced by various masks to be able to select the size of the exposed areas, referred to in the following sections as the *occupancy*, as well as the level of illumination of individual modules. For the measurements requiring flat-field-like illumination from copper fluorescence, the mask shown in Figure 3B was used. It consists of two vertical tantalum bars, each 19 mm wide and 2 mm thick, which shadowed a large fraction of each module. A typical image collected in such a configuration is presented in Figure 3D. Pixels behind the bars were used, mostly, to determine the baseline-shift corrections. The JNGFR04 served as an incident intensity monitor. A stack of

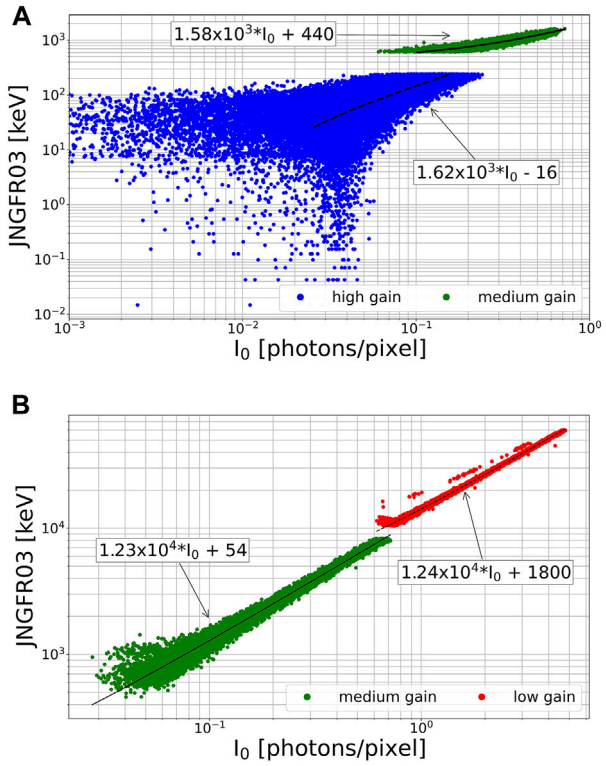

FIGURE 4
Examples of the intensity scans across **(A)** high to medium and **(B)** medium to low transition regions measured in the first image of the burst. The response of the pixel in different gain stages have each been fitted with linear functions, and fit results are shown in the plots. In order to access both transition regions, the scans were performed in two different experimental arrangements. Therefore values of the normalized I_0 in the two plots should not be compared directly.

aluminum foils (not shown in the figure) was placed in front of it to adjust the average intensity of photons per pixel to the desired levels. The mask shown in Figure 3C was used to study the correlation between the occupancy levels and performance of the JUNGFRAU modules, especially across the transition regions. It consists of two sets of panels with 1 mm and 8 mm holes. The position of the holes with respect to ASICs was optimized by adjusting the position of each detector half as well as the position of the mask itself. An example image acquired with this mask is shown in Figure 3E.

In order to measure, in relative terms, the intensity of the fluorescence signal on the detector, one of the eight modules was used as an intensity (I_0) monitor for each measurement. The module was shielded with an aluminum foil so that the intensity of the transmitted fluorescence photons reaching the module itself would always be at a sufficiently low intensity to allow the module not to switch gain but to remain in the independently calibrated G0 region; the I_0 value is then presented as the average number of photons per pixel behind the foil. Consequently, the thickness of the aluminum absorber has been changed to keep the overall maximum signal on the I_0 module at the same level, for each individual measurement. So it is important to keep in mind that the I_0 values from measurements obtained in severely different illumination conditions cannot be compared directly.

The data presented in this report was collected during multiple experiments. The experimental setup during each session was adjusted to accommodate the goals of the particular measurements as well as the current configuration of the SPB/SFX instrument but the core set of parameters was preserved across all the activities. All data were acquired in the transmission geometry using the fluorescence from a 5 µm-thick copper foil. The size of the 9.3 keV beam at the interaction point was set to approximately 400 × 400 µm^2. The incident flux was tuned with the help of diamond filters, providing up to 64 different attenuation levels with the smallest step of 7%. Contamination from the 9.3 keV air scattering at low angles was reduced by placing a 15 µm-thick nickel foil downstream of the interaction point. The sample-to-detector distance was adjusted for each type of measurement between 120 and 500 mm to find the best compromise between the flatness of the signal across the entire detector and the maximum number of photons per pixel. For larger distances, an additional He-filled pipe was installed to further suppress the air scattering.

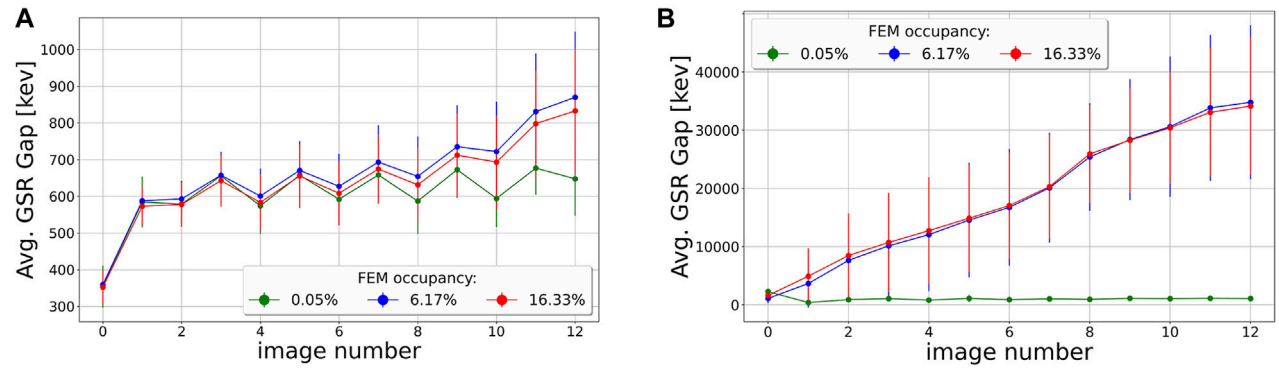

FIGURE 5
Average 'gap' value for a FEM vs. memory cell. Values are plotted as a function of the order in which images are stored during the burst, for different occupancy levels. In **(A)** the values for the GSR between G0 and G1 are plotted, while **(B)** shows values for the gain switching region between G1 and G2. A slight dependency on occupancy can be noted for the first GSR, while the effect is evident in the second GSR, where the absolute signal on the detector is ten times higher.

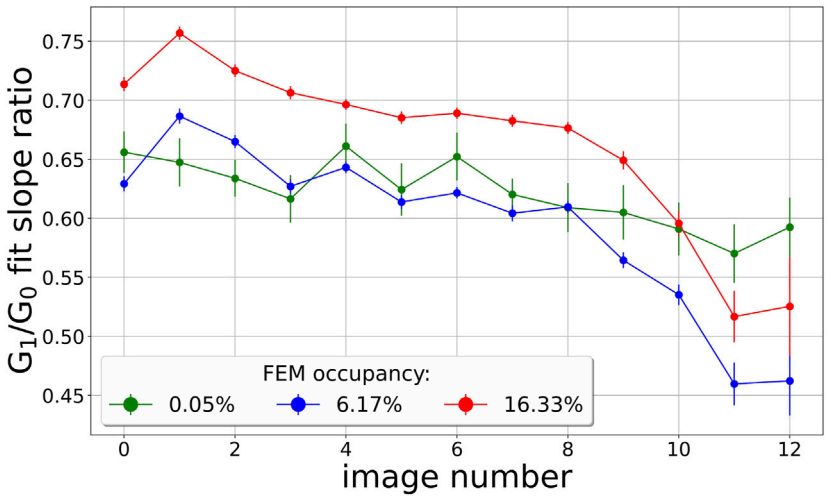

FIGURE 6
The average value for a FEM for the ratio between the slope of the G1 and the G0 part of the intensity scan is displayed. The error bars indicate the RMS of the distribution of values across the pixels.

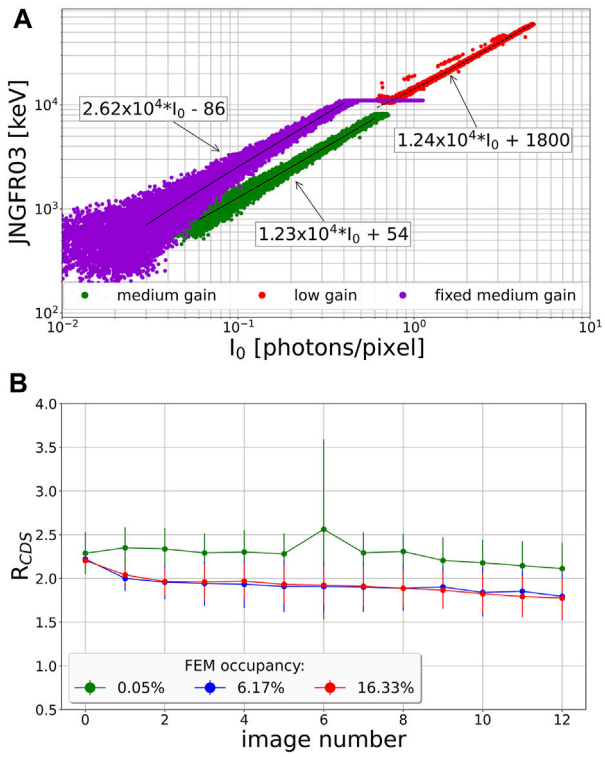

FIGURE 7
In **(A)** the output of an intensity scan in fixed medium gain (fixG1) is compared with a scan taken in the dynamic gain switching (DGS). Both scans were carried out under the same experimental conditions. The difference in slope of the lines is due to the intercalibration factor R_{CDS}. Impact of the occupancy level on the value of R_{CDS} is shown in **(B)**.

Prior to the intensity scans, the detector G0 stage was calibrated using Cu K_α fluorescence photons at an intensity low enough so that individual photons could be resolved; the gain conversion factors for the G1 and G2 stages with respect to G0 were calculated for each pixel and memory cell, with a procedure similar to what is described in [19].

2.3 Experimental tests in *burst* mode

Based on the promising results obtained from the *burst* mode characterization, the performance of the detector was validated against data collected in single cell mode. Two experiments were conducted, each utilizing the detector at very different photon intensity levels and signal distribution across the sensors. For reasons outlined in Section 3, the operation of the detector in *burst* mode was restricted to the fixed G1 stage. The lack of absolute gain calibration for this detector setting did not pose a major problem for these measurements.

2.3.1 Serial femtosecond crystallography

In this section, we describe the SFX test experiment using the JF4M detector in *burst* mode with the gain set to fixed medium gain. One of the calibration samples used routinely at the SPB/SFX instrument was chosen; crystals of the hen egg-white lysozyme (HEWL) with a diameter of 2–3 µm. Crystals were grown using the well-established protocol [22] and injected into the interaction point beam as a liquid jet using a Gas Dynamic Virtual Nozzle (GDVN) type B, as described in [23], with a sample flow rate of 70 µL/min. To minimize the air scattering background, the sample chamber enclosing the interaction point was continuously flushed with helium. The crystals were exposed to a 12.55 keV X-ray beam focused to a 3 µm spot. The detector was positioned 118.3 mm downstream from the interaction point. This configuration corresponded to the maximum resolution of 1.6/1.5 Å at the edges/corner of the detector. Both photon energy and sample-to-detector distance were refined from the SFX data based on expected unit cell parameters of the HEWL crystals.

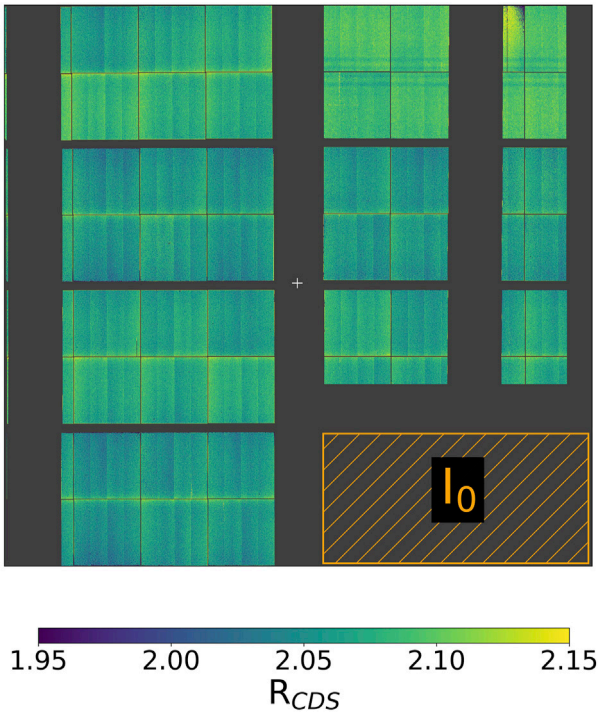

FIGURE 8
The R_{CDS} factor for the first memory cell, obtained from a flat field intensity scan of the JF4M is shown. The vertical dark stripes in the image are the portions of the detector covered by tantalum bars and mask holder. The module used for the incident intensity normalization as well as part of the other module shadowed by the aluminum foils (see the Section 2.2.1 for details) were also masked out.

2.3.2 Kossel line measurement

When fluorescent radiation emitted by the atoms in a single crystal is scattered by the crystal itself, intensity modulations, so-called Kossel lines, can be observed in the diffraction intensity [24]. As the phase of the structure factor is encoded in the profiles of those lines, and a single image contains multiple lines, complex insight into the structure of the illuminated crystal can be gained from the analysis of a single diffraction pattern. Measurement of the Kossel lines can be a way to overcome constraints faced by techniques relying on the accumulation of thousands of images such as serial femtosecond crystallography [22] or single particle imaging [25]. Access to such rich information about the structural changes within a sample from a single pulse is critical for pump-probe-type experiments, especially when the given pumped state of the sample cannot be easily repeated thousands of times. The MHz repetition rate of the EuXFEL enables the tracing of changes in sample structure with sub-µs resolution. To support this type of measurement, the detector needs to meet stringent conditions. First, it has to allow measurements of the profiles of the Kossel lines with sufficient spatial resolution on top of the fluorescent background. Second, it has to be fast enough to take advantage of the MHz intra-bunch repetition rate. The JUNGFRAU detector, operated in *burst* mode, has suitable specifications for this use case, at least within the 150 kHz limit highlighted before.

Proof-of-principle single-pulse Kossel line measurements were recently conducted at the SPB/SFX instrument using the JF4M detector. Here, the feasibility of the *burst* mode to measure Kossel lines for one demonstration sample, a 100 µm thick Ge crystal, is reported. The single crystal Ge wafer was illuminated by a series of 16 pulse bursts of 11.5 keV beam focused down to 25 µm × 25 µm. For each burst, a fresh spot of the wafer was exposed. The X-ray beam energy at the sample position was adjusted using diamond foils to several µJ, which was sufficient to observe the Kossel lines in several images before the radiation damage-induced signal dominated in the recorded patterns. The alignment of the wafer and the quality of its surface were monitored with the help of a microscope, inline with the X-ray illumination. Data were acquired in transmission geometry with the detector positioned 120 mm from the interaction point. To reduce air scattering contamination, the sample was encapsulated in a He-flushed chamber.

Based on measurements taken in the single memory cell configuration, for which the absolute calibration was available, the number of 9.25 keV fluorescent photons per pixel per pulse ranged from 20/120 to 200/800 at the edges/center of the detector. The exposure time was set to 20.12 µs to provide the desired time resolution for this measurement.

3 Results

3.1 Intensity scan results

Various intensity scans were conducted in *burst* mode in both DGS as well as in fixed gain. Results are summarized in the following sections.

3.1.1 Gain switching region gap

It became immediately evident that the pedestal evaluation via forced switching of the feedback capacitor of the pre-amplifier shows substantial limitations in accuracy. This manifests itself as a positive 'gap' in the GSR. It indicates that this method underestimates the actual pedestal value after gain switching occurs. An example of the intensity scan for a pixel of JNGFR03 module is shown in Figure 4.

The value of this 'gap' can be estimated by calculating the difference between the lowest value in G1 and the highest in G0: the average 'gap' value per memory cell and per module shows a clear incremental trend with the memory cell filling order. However, when looking for dependencies of this value on the total occupancy of the FEM, a minimal effect has been noted for the first GSR (see Figure 5A), while the effect is evident when inspecting the GSR between G1 and G2 (Figure 5B), where a strong dependency is evident, on both occupancy and filling order of the memory cell.

3.1.2 Gain calibration

The results concerning the validation of the gain calibration are presented in the subsequent paragraphs, for the DGS and the fixed gain operation separately.

3.1.2.1 Lower gains in dynamic gain switching

The corrected output of the intensity scan as a function of I_0 has been fitted with linear functions for each pixel, cell and gain stage. An example can be seen in Figure 4. As mentioned in Section 2.1.2.1.2, the ratio of the slopes of the G1 and the G0 parts of the intensity scan, $G1_{DGS}$ and $G0_{DGS}$, should be equal to 1. Instead, we

TABLE 1 SFX data and refinement statistics.

Parameter	Value
Photon energy (eV)	12,550
X-ray focus, FWHM (μm)	3
Electron bunch length (fs)	24
Frame count	97,128
Indexed crystals	18,420
Indexing rate (%)	18.96
Space group	$P4_32_12$
Point group	4/mm
Cell dimensions (Å)	
a	79.75
b	79.75
c	38.60
Resolution	17.91–1.55 (1.6–1.55)
R_{split}	10.72 (60.21)
$CC_{1/2}$	98.14 (63.32)
SNR	6.84 (1.26)
Completeness	100 (100)
Multiplicity	241.7 (113.3)
No. reflections (R free set)	18,039 (902)
R_{work}/R_{free}	0.1808/0.1976
Bond length (Å)	0.005
Bond angle (°)	0.883
Ramachandran	
favored/allowed/outlier	99.21/0.79/0.0
Average B-factor	22.53

Data were acquired in the fixed medium gain and using a single X-ray pulse per exposure. Due to restrictions on the time window, only the first eight memory cells were illuminated.

found that, on average, it is substantially different from unity. The values of the slope ratios of G1 and G0 on a module level show that the gain conversion factor for medium gain in DGS mode is overestimated by approximately 30% when we assume that gain ratios calculated in single cell mode will hold true for all storage cells. In Figure 6, the module average per memory cell is shown; the results are plotted according to the order in which the memory cells are filled during a burst. It can clearly be noted that not only is the ratio substantially lower than unity, but there appears to be a decreasing trend with filling order. No clear dependence on the FEM occupancy appears from the data.

3.1.2.2 Fixed medium gain

Operation in *burst* mode in fixed medium gain (fixG1) presents fewer calibration challenges. On top of the obvious absence of a GSR with the resulting pedestal evaluation difficulties highlighted in the previous paragraph, an absolute gain calibration is not necessary to maintain a linear response across its entire dynamic range (Figure 7A). Thus fixed gain setting appears to be a more straightforward candidate for *burst* operation mode.

As mentioned in Section 2.1.1, the CDS stage is not bypassed in fixed gain, hence the gain conversion factor calculated for G1 in DGS does not provide a full correction. To test the possibility to cross-calibrate the two factors (and hence measure the amplification provided by the CDS stage), the intensity scans in fixG1 have been corrected with the gain factor calculated for DGS. Data has been fitted with linear functions and the intercalibration factor R_{CDS} was estimated using the formula:

$$R_{CDS} = \mathrm{G1}_{fix} \big/ \mathrm{G1}_{DGS}. \tag{3}$$

The average values of R_{CDS} as a function of the memory cell number for various occupancy levels are plotted in Figure 7B. Results indicate a weak dependence of the R_{CDS} factor on the memory cell, while the total amount of signal in the FEM has to be taken into account when estimating the values of R_{CDS}. At this point, it has to be stressed that each occupancy level data set was collected for a different module. To verify to what extent the observed trends can be explained by the unique characteristics of the individual modules, the intensity scans were repeated in the flat-field illumination geometry using the mask shown in Figure 3B. As presented in Figure 8, the values of the R_{CDS} factor are similar across all the modules and consistent with the lower occupancy level data (Figure 7B).

3.2 First experiments

Due to the issues encountered in the characterization of the operation of the JUNGFRAU detector in *burst* mode with DGS, and the promising results during *fixed gain* operation, the experimental tests of SFX and Kossel line measurement have been performed without the DGS mechanism. These types of measurements represent different regimes of detector operation. In the case of SFX, diffracted photons are confined, mostly, to clusters of pixels. The accumulated charge varies among the clusters by few orders of magnitude. Resolving Kossel lines requires the detection of small signals superimposed by a large, uniform background. In the following sections, we show that *burst* mode operation in fixed gain can be used in both scenarios.

3.2.1 Serial femtosecond crystallography

For this particular experiment, an exposure time of 12.7 μs and a single X-ray pulse per frame were chosen. The accelerator was configured to produce 24 fs electron bunches. Although all 16 memory cells were used only the first 8 memory cells were illuminated by X-rays, due to the limited RF-window available for this particular experiment. Diffraction patterns were processed with the CrystFEL software [26] with PEAKFINDER8 and XGANDALF used for peakfinding and indexing, respectively. The PHENIX package [27] was then used to perform molecular replacement (with PDB 6FTR as search model) and structure refinement. Data from 97,128 bursts was acquired in two 10 min data sets. In total, 18,420 crystals were identified with an indexing rate of 18.96%,

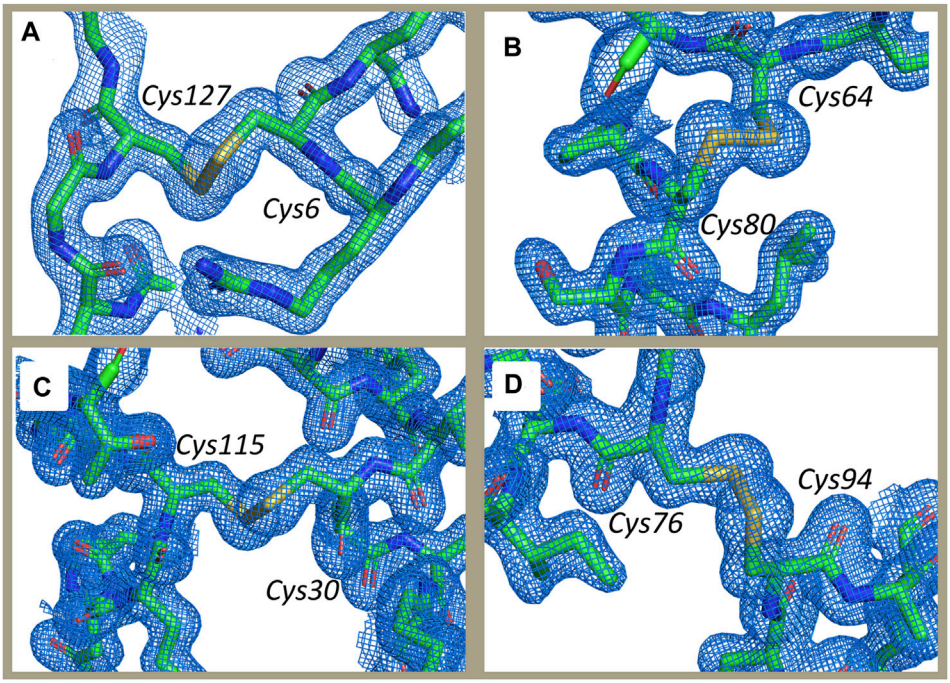

FIGURE 9
The electron density maps around the four disulfide bonds area in the hen egg-white lysozyme. Regions around cysteines 6 and 127 **(A)**, 64 and 80 **(B)**, 30 and 115 **(C)**, 76 and 94 **(D)** display continuous densities. The 2Fo-Fc map is shown in blue at 1σ using PyMOL version 2.3.0 (ref: The PyMOL Molecular Graphics System, Version 2.3 Schroedinger, LLC).

only counting the illuminated frames. The figures of merit showing very good statistics and outcome of the structure refinement are summarized in Table 1. The obtained electron density map at 1.55 Å resolution appears free from local radiation damage as illustrated by the well-defined disulfide bond areas and presented in Figure 9. Distribution of the indexed frames across the illuminated memory cells is shown in Figure 10. As desired, the indexed patterns are uniformly distributed among the first eight cells, while no crystals were identified in any of the "dark" cells, which indicates a lack of cross-talk between the memory cells.

3.2.2 Kossel line measurement

Example data from a single 16-pulse burst showing the evolution of the Kossel lines as function of the radiation dose are presented in Figure 11. Despite the large intensity gradient in the collected images, the Kossel lines can clearly be resolved on the single-pulse level. Visibility of the lines increased as a function of the pulse number in the burst, reflecting the change of the mesoscopic structure of the sample. With the 120 mm sample-to-detector distance, the sensitive area of the detector covered a sufficient fraction of the Kossel line pattern to solve the 3D crystalline structure of the sample but the resolution of the fine structure of the lines was limited. With increasing accumulated dose towards the end of the burst, radiation damage of the wafer becomes evident, which is reflected by the sharp Bragg peaks from polycrystalline Ge. For future experiments, the quality of the data could be greatly improved by thinning the sample, switching to the backscattering geometry, and extending the sample-to-detector distance. However, the outcome of this experiment proved the feasibility of pulse-resolved Kossel line measurements at the European XFEL. Most importantly, it showed

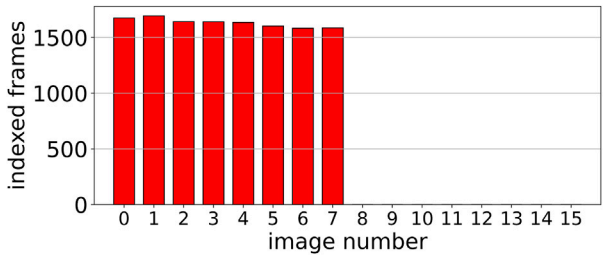

FIGURE 10
Number of the indexed crystals per memory cell for the serial femtoseconds crystallography data set form the hen egg-white lysozyme collected in the *burst* mode and fixed medium gain. Only the first eight frames were illuminated and the rest was kept dark.

that the JUNGFRAU detector operated in *burst* mode is a well-suited tool to support such demanding measurements at kHz time-scales.

4 Discussion

These characterization results indicate that the operation of the JUNGFRAU detector in *burst* mode with DGS requires a new calibration procedure in order to properly correct the raw output after gain switching:

- The current pedestal evaluation for the G1 and G2 gain stages through forced gain switching does not produce predictive results;

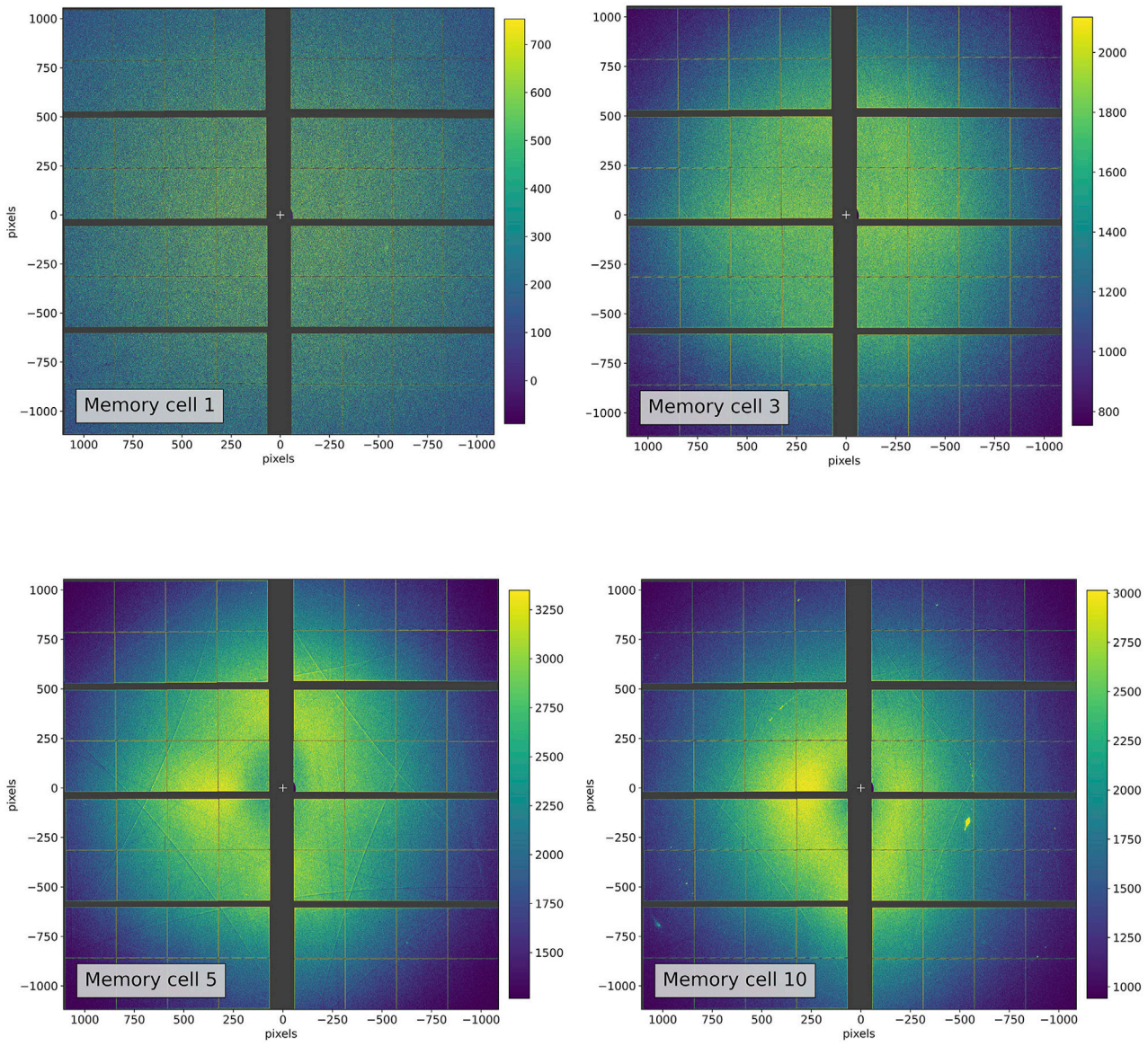

FIGURE 11
The Kossel lines measured for 100 µm thick Ge single crystal using the JUNGFRAU detector in fixed medium gain configuration. Photon energy of the incident radiation was set to 11.5 keV. The sample was illuminated by a single X-ray pulse per each 20.12 µs exposure. Visibility of the lines improves with increasing accumulated dose. Eventually, the polycrystalline Ge becomes well-pronounced.

- The gain ratios R_1 and R_2 estimated for *single cell* operation do not accurately predict the gain conversion factors for lower gain stages. These are overestimated by ~30%, with a dependency on the order in which the memory cells are filled. This indicates that we could experience one (or more) of the following effects:

1. As well as the $G0_{burst}$ gain being lower than expected due to the memory cell read/write operation, the feedback capacitance of the pre-amplifier in $G0_{burst}$ is lower than predicted. This could be due to additional parasitic capacitances coming from the different way in which the pixel is operated in burst mode.
2. It is not possible to completely preset the pre-amplifier charge in between images during the burst, which will introduce inter-cell mixing effectively resulting in a lower gain.

Dedicated measurements are planned to understand the issue in detail.

Operation at photon fluxes so low that gain switching is not triggered does not seem to present particular calibration issues.

Concerning *fixed gain* operation, no issue with the pedestal evaluation has been noticed, while the issue of calculating the intercalibration factors R_{CDS} for each pixel and memory cell remains unresolved. It is however worth stressing that in the

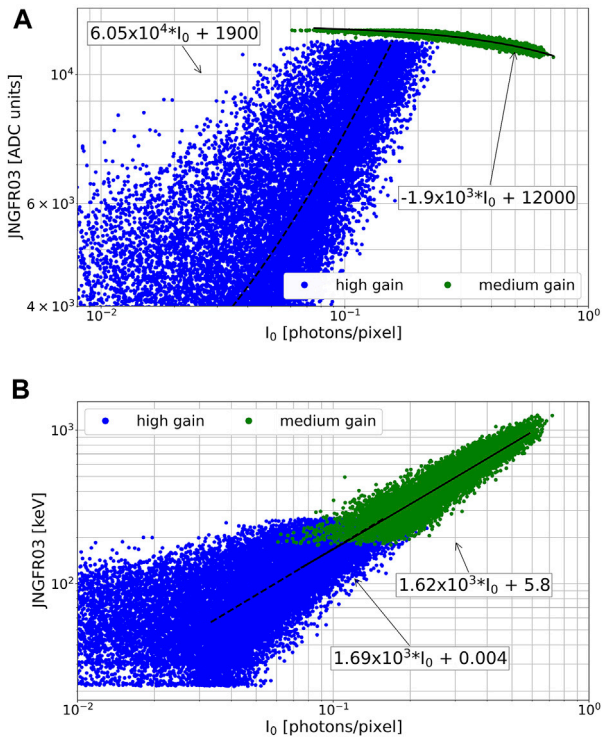

FIGURE 12
Examples of closed loop correction. In **(A)** the raw output for the same pixel and memory cell shown inf Figure 4A is shown, while in **(B)** the corrected output obtained using the results of the linear fits shown in **(A)**.

experimental tests conducted in *fixed gain*, the absence of an absolute gain calibration did not impact the successful results, as presented in Sections 3.2.1 and 3.2.2.

4.1 Prospects for calibration strategies

4.1.1 Pedestal calibration

At the moment two possible calibration strategies for pedestal evaluation are being envisaged:

1. Gap correction: continue using the forced gain switch for pedestal estimate and apply an additional correction for the 'gap';
2. Linear fit estimate: fit with a linear function the raw output of the intensity scan, and use the linear function offset fit parameter as an estimate of the pedestal, in a similar way to the closed loop correction described in [20].

An example of the results obtained using *linear fit estimates* of offset is shown in Figure 12. There, the same data are shown as in Figure 4A, however they have been corrected with the results of the fit of the raw output, and as a result the 'gap' is closed and the slopes align.

Since the re-calibration of the pedestal via an intensity scan is not practical in many experimental situations, the calibration constants produced via both the methods proposed above need to be tested for their portability, their dependence on temperature and exposure time. Results will be presented in subsequent communications.

4.1.2 Gain calibration

It is evident that *burst* operation mode in DGS requires a re-calibration of the gain conversion factors R_1 and R_2, in order to maintain a linear response through the whole dynamic range. For this purpose, the method described in (19), must be applied to the detector when operating in *burst* mode. In addition, the dynamic range scans necessary to calculate R_1 and R_2 may also be employed to extract information about the pedestal position for lower gain stages.

Concerning *fixed gain* operation, instead, the calculation of R_{CDS} is not fundamental to maintain a linear response, and it is useful only if absolute gain calibration is needed. If this would be the case, the intercalibration factor can be calculated using dynamic range scans with photons, or external charge injection. Dependence of the R_{CDS} as function of occupancy levels or memory cell did not impact the quality of the presented scientific data. Additional calibration of the gains, may be required when the total signal within the images would fluctuate by several orders of magnitude.

4.2 Experimental tests in fixed gain

The results obtained with the detector operated in *burst* mode with *fixed gain* settings prove that the detector can produce scientifically relevant results. At present this operation mode is limited to cases where the absolute gain calibration is not critical for the experimental outcome, but a seemingly straightforward gain intercalibration presents a good prospect to further widen the range of accessible experiments.

4.3 Conclusions

The calibration strategy proposed in Section 2.1.2.1 for the JUNGFRAU DGS mechanism in *burst* operation mode has been put to test extensively. Results indicate that forced gain switching produces a largely underestimated evaluation of the pedestal for the lower gains (G1 and G2), which results in strong artificial discontinuities in the corrected data. Concerning the gain calibration, the assumption that the ratio between feedback capacitors estimated with the *single cell* calibration procedure should remain valid leads to an overestimation of the actual gain conversion factor.

Both these results indicate the need to re-think the calibration procedure required for *burst* operation mode with DGS mechanism: the possibility of using dynamic range scans as outlined in Section 4.1 seems promising, but the method needs to be validated and tested most of all against the stability of its results. The outcome of this study will be presented in future communications.

On the other hand, the operation in *fixed gain* seems not to present major obstacles to its usage in experiments. Two separate tests have been conducted, namely, protein crystallography and Kossel line measurements. The results validated the data produced by the JUNGFRAU detector in *burst* mode and showed benefits of this mode in making better use of the EuXFEL pulse train structure, although compromises are needed on the dynamic range.

Besides benefiting SFX, implementations of this fixed-gain operation mode of JUNGFRAU will be relevant for many experimental techniques utilized at the European XFEL. For

example, ultrafast X-ray diffraction experiments, where the intensity and position of a Bragg peak are monitored as a function of laser excitation, will allow pulse-resolved measurements to be performed at up to 16 pulses per train, providing better signal-to-noise ratio and statistics on compatible samples. As the Bragg diffraction intensity does not vary over several orders of magnitude between pulses, these measurements do not necessarily require the DGS capabilities for data collection. A similar method will also work for time-resolved X-ray emission spectroscopy (XES) measurements, where the per-pulse X-ray signals are often weak, allowing a fixed gain mode to be defined for data collection. This approach will allow XES measurements to take advantage of the excellent low noise characteristics of the JUNGFRAU detector, while benefiting from the pulse-resolved measurement capabilities. This latter ability will allow interleaved laser excitation, where every second X-ray pulse in the train is laser-excited, resulting in significant improvements in the signal-to-noise ratio of laser ON - laser OFF differences due to the better intra-train stability of the X-ray parameters compared to the inter-train stability. Many pump-probe experiments require the highest possible laser powers, which are often achieved at the cost of repetition rates reduced to a few hundreds of kHz. In those cases, the *burst* mode of JUNGFRAU becomes an attractive option.

Data availability statement

The raw data supporting the conclusion of this article will be made available by the authors, without undue reservation.

Author contributions

MR: Conceptualization, Data curation, Formal Analysis, Investigation, Methodology, Validation, Writing–original draft, Writing–review and editing. MS: Conceptualization, Data curation, Formal Analysis, Investigation, Methodology, Validation, Writing–original draft, Writing–review and editing. RW: Formal Analysis, Methodology, Software, Validation, Writing–review and editing. VH: Conceptualization, Methodology, Supervision, Writing–review and editing. AM: Conceptualization, Methodology, Supervision, Writing–review and editing. BS: Conceptualization, Investigation, Supervision, Writing–review and editing. HH: Resources, Writing–review and editing. RB: Writing–review and editing, Project administration, Resources. JB: Resources, Writing–review and editing. GB: Conceptualization, Formal Analysis, Methodology, Resources, Writing–review and editing. TD: Resources, Writing–review and editing. GF: Conceptualization, Formal Analysis, Methodology, Resources, Writing–review and editing. KK: Resources, Writing–review and editing. CK: Resources, Writing–review and editing. JK: Resources, Writing–review and editing. FK: Resources, Writing–review and editing. RL: Resources, Writing–review and editing. LL: Resources, Writing–review and editing. NR: Resources, Writing–review and editing. AR: Writing–review and editing. AS: Resources, Writing–review and editing. TS: Resources, Writing–review and editing. MiT: Conceptualization, Formal Analysis, Methodology, Resources, Writing–review and editing. MoT: Supervision, Writing–review and editing.

Funding

The author(s) declare financial support was received for the research, authorship, and/or publication of this article. This work was funded by Wellcome Trust grant. Bundesministerium für Bildung und Forschung grants 05K13GU7; and 05E13GU1. Ministerstvo školstva, vedy, výskumu a športu Slovenskej republiky grant. Svenska Forskningsrådet Formas grant 822-2013-2014. Knut och Alice Wallenbergs Stiftelse grant. Röntgen-Ångström Cluster grant. Stiftelsen för Strategisk Forskning grant. Australian Research Council Center of Excellence in Advanced Molecular Imaging grant CE140100011. Australian Nuclear Science and Technology Organisation grant. Max-Planck-Gesellschaft grant. Helmholtz Association grant. MSCA PSI-FELLOW-III-3i (EU Grant Agreement No. 884104).

Acknowledgments

The authors would like to acknowledge the contribution of the European XFEL and in particular of the scientific instruments SPB/SFX for the beam time allocations, preparation and support during operation.

Conflict of interest

The authors declare that the research was conducted in the absence of any commercial or financial relationships that could be construed as a potential conflict of interest.

Publisher's note

References

1 . Mozzanica A, Andrä M, Barten R, Bergamaschi A, Chiriotti S, Brückner M, et al. The JUNGFRAU detector for applications at synchrotron light sources and XFELs. *Synchrotron Radiat News* (2018) 31:16–20. doi:10.1080/08940886.2018.1528429

2 . Mozzanica A, Bergamaschi A, Cartier S, Dinapoli R, Greiffenberg D, Johnson I, et al. Prototype characterization of the JUNGFRAU pixel detector for SwissFEL. *J Instrumentation* (2014) 9:C05010. doi:10.1088/1748-0221/9/05/c05010

3 . Mozzanica A, Bergamaschi A, Brueckner M, Cartier S, Dinapoli R, Greiffenberg D, et al. Characterization results of the JUNGFRAU full scale readout ASIC. *J Instrumentation* (2016) 11:C02047. doi:10.1088/1748-0221/11/02/C02047

4 . Decking W, Abeghyan S, Abramian P, Abramsky A, Aguirre A, Albrecht C, et al. A MHz-repetition-rate hard X-ray free-electron laser driven by a superconducting linear accelerator. *Nat Photon* (2020) 14:391–7. doi:10.1038/s41566-020-0607-z

5 . Allahgholi A, Becker J, Delfs A, Dinapoli R, Goettlicher P, Greiffenberg D, et al. The adaptive gain integrating pixel detector at the European XFEL. *J Synchrotron Radiat* (2019) 26:74–82. doi:10.1107/S1600577518016077

6 . Wheater R, Hart M, Veale M, Wilson M, Doblas-Jiménez D, Turcato M, et al. Development of data correction for the 1M large pixel detector at the EuXFEL. *J Instrumentation* (2022) 17:P04013. doi:10.1088/1748-0221/17/04/P04013

7 . Porro M, Andricek L, Aschauer S, Castoldi A, Donato M, Engelke J, et al. The MiniSDD-based 1-mpixel camera of the DSSC Project for the European XFEL. *IEEE Trans Nucl Sci* (2021) 68:1334–50. doi:10.1109/TNS.2021.3076602

8 . Mezza D, Allahgholi A, Delfs A, Dinapoli R, Goettlicher P, Graafsma H, et al. New calibration circuitry and concept for AGIPD. *J Instrumentation* (2016) 11:C11019. doi:10.1088/1748-0221/11/11/C11019

9 . Mezza D, Becker J, Carraresi L, Castoldi A, Dinapoli R, Goettlicher P, et al. Calibration methods for charge integrating detectors. *Nucl Instr Methods Phys Res Section A: Acc Spectrometers, Detectors Associated Equipment* (2022) 1024:166078. doi:10.1016/j.nima.2021.166078

10 . Tolstikova A, Levantino M, Yefanov O, Hennicke V, Fischer P, Meyer J, et al. 1 kHz fixed-target serial crystallography using a multilayer monochromator and an integrating pixel detector. *IUCrJ* (2019) 6:927–37. doi:10.1107/S205225251900914X

11 . Preston T, Göde S, Schwinkendorf JP, Appel K, Brambrink E, Cerantola V, et al. Design and performance characterisation of the HAPG von Hámos spectrometer at the high energy density instrument of the European XFEL. *J Instrumentation* (2020) 15: P11033. doi:10.1088/1748-0221/15/11/P11033

12 . Milne CJ, Schietinger T, Aiba M, Alarcon A, Alex J, Anghel A, et al. SwissFEL: the Swiss X-ray free electron laser. *Appl Sci* (2017) 7:720. doi:10.3390/app7070720

13 . Redford S, Bergamaschi A, Brückner M, Cartier S, Dinapoli R, Ekinci Y, et al. Calibration status and plans for the charge integrating JUNGFRAU pixel detector for SwissFEL. *J Instrumentation* (2016) 11:C11013. doi:10.1088/1748-0221/11/11/C11013

14 . Khakhulin D, Otte F, Biednov M, Bömer C, Choi TK, Diez M, et al. Ultrafast X-ray photochemistry at European XFEL: capabilities of the femtosecond X-ray experiments (FXE) instrument. *Appl Sci* (2020) 10:995. doi:10.3390/app10030995

15 . Bacellar C, Kinschel D, Mancini GF, Ingle RA, Rouxel J, Cannelli O, et al. Spin cascade and doming in ferric hemes: femtosecond X-ray absorption and X-ray emission studies. *Proc Natl Acad Sci* (2020) 117:21914–20. doi:10.1073/pnas.2009490117

16 . Šmíd M, Baehtz C, Pelka A, Laso García A, Göde S, Grenzer J, et al. Mirror to measure small angle x-ray scattering signal in high energy density experiments. *Rev Scientific Instr* (2020) 91:123501. doi:10.1063/5.0021691

17 . Voigt K, Zhang M, Ramakrishna K, Amouretti A, Appel K, Brambrink E, et al. Demonstration of an x-ray Raman spectroscopy setup to study warm dense carbon at the high energy density instrument of European XFEL. *Phys Plasmas* (2021) 28:082701. doi:10.1063/5.0048150

18 . Kaa JM, Konôpková Z, Preston TR, Cerantola V, Sahle CJ, Förster M, et al. A von Hámos spectrometer for diamond anvil cell experiments at the high energy density instrument of the European X-ray free-electron laser. *J Synchrotron Radiat* (2023) 30: 822–30. doi:10.1107/S1600577523003041

19 . Redford S, Andrä M, Barten R, Bergamaschi A, Brückner M, Dinapoli R, et al. First full dynamic range calibration of the JUNGFRAU photon detector. *J Instrumentation* (2018) 13:C01027. doi:10.1088/1748-0221/13/01/c01027

20 . Redford S, Andrä M, Barten R, Bergamaschi A, Brückner M, Chiriotti S, et al. First full dynamic range scan of the JUNGFRAU detector performed at an XFEL with an accurate intensity reference. *J Instrumentation* (2020) 15:C02025. doi:10.1088/1748-0221/15/02/c02025

21 . Mancuso AP, Aquila A, Batchelor L, Bean RJ, Bielecki J, Borchers G, et al. The single particles, clusters and biomolecules and serial femtosecond crystallography instrument of the European XFEL: initial installation. *J Synchrotron Radiat* (2019) 26:660–76. doi:10.1107/S1600577519003308

22 . Boutet S, Lomb L, Williams GJ, Barends TR, Aquila A, Doak RB, et al. High-resolution protein structure determination by serial femtosecond crystallography. *Serial Femtosecond Crystallogr* (2012) 337:362–4. doi:10.1126/science.1217737

23 . Vakili M, Vasireddi R, Gwozdz PV, Monteiro DCF, Heymann M, Blick RH, et al. Microfluidic polyimide gas dynamic virtual nozzles for serial crystallography. *Rev Scientific Instr* (2020) 91:085108. doi:10.1063/5.0012806

24 . Faigel G, Bortel G, Tegze M. Experimental phase determination of the structure factor from kossel line profile. *Scientific Rep* (2016) 6:22904. doi:10.1038/srep22904

25 . Bielecki J, Maia FRNC, Mancuso AP. Perspectives on single particle imaging with x rays at the advent of high repetition rate x-ray free electron laser sources. *Struct Dyn* (2020) 7:040901. doi:10.1063/4.0000024

26 . White TA, Kirian RA, Martin AV, Aquila A, Nass K, Barty A, et al. CrystFEL: a software suite for snapshot serial crystallography. *J Appl Crystallogr* (2012) 45:335–41. doi:10.1107/S0021889812002312

27 . Adams PD, Afonine PV, Bunkóczi G, Chen VB, Davis IW, Echols N, et al. PHENIX: a comprehensive Python-based system for macromolecular structure solution. *Acta Crystallogr Section D* (2010) 66:213–21. doi:10.1107/S0907444909052925